PHYSICAL REVIEW D **71,** 122003 (2005)

White-dwarf–white-dwarf galactic background in the LISA data

Jeffrey A. Edlund* and Massimo Tinto†
Jet Propulsion Laboratory, California Institute of Technology, Pasadena, California 91109, USA

Andrzej Królak‡
Max-Planck-Institute for Gravitational Physics, Albert Einstein Institute, D-14476 Golm, Germany

Gijs Nelemans§
Department of Astrophysics, IMAPP, Radboud University Nijmegen, The Netherlands
(Received 21 April 2005; published 20 June 2005)

LISA (Laser Interferometer Space Antenna) is a proposed space mission, which will use coherent laser beams exchanged between three remote spacecraft to detect and study low-frequency cosmic gravitational radiation. In the low part of its frequency band, the LISA strain sensitivity will be dominated by the incoherent superposition of hundreds of millions of gravitational wave signals radiated by inspiraling white-dwarf binaries present in our own Galaxy. In order to estimate the magnitude of the LISA response to this background, we have simulated a synthesized population that recently appeared in the literature. Our approach relies on entirely analytic expressions of the LISA time-delay interferometric responses to the gravitational radiation emitted by such systems, which allows us to implement a computationally efficient and accurate simulation of the background in the LISA data. We find the amplitude of the galactic white-dwarf binary background in the LISA data to be modulated in time, reaching a minimum equal to about twice that of the LISA noise for a period of about two months around the time when the Sun-LISA direction is roughly oriented towards the Autumn equinox. This suggests that, during this time period, LISA could search for other gravitational wave signals incoming from directions that are away from the galactic plane. Since the galactic white-dwarf background will be observed by LISA not as a stationary but rather as a cyclostationary random process with a period of 1 yr, we summarize the theory of cyclostationary random processes, present the corresponding generalized spectral method needed to characterize such process, and make a comparison between our analytic results and those obtained by applying our method to the simulated data. We find that, by measuring the generalized spectral components of the white-dwarf background, LISA will be able to infer properties of the distribution of the white-dwarf binary systems present in our Galaxy.

DOI: 10.1103/PhysRevD.71.122003 PACS numbers: 04.80.Nn, 07.60.Ly, 95.55.Ym

I. INTRODUCTION

The Laser Interferometric Space Antenna (LISA) is a space mission jointly proposed to the National Aeronautics and Space Administration (NASA) and the European Space Agency. Its aim is to detect and study gravitational waves (GW) in the millihertz frequency band. It will use coherent laser beams exchanged between three identical spacecraft forming a giant (almost) equilateral triangle of side 5×10^6 km. By monitoring the relative phase changes of the light beams exchanged between the spacecraft, it will extract the information about the gravitational waves it will observe at unprecedented sensitivities [1].

The astrophysical sources that LISA is expected to observe within its operational frequency band (10^{-4}–1 Hz) include extragalactic supermassive black-hole coalescing binaries, stochastic gravitational wave background from the early Universe, and galactic and extragalactic coalescing binary systems containing white dwarfs and neutron stars.

Recent surveys have uniquely identified 20 binary systems emitting gravitational radiation within the LISA band, while population studies have concluded that the large number of binaries present in our own Galaxy should produce a stochastic background that will lie significantly above the LISA instrumental noise in the low part of its frequency band. It has been shown in the literature (see [2] for a recent study and [3,4] for earlier investigations) that these sources will be dominated by detached white-dwarf–white-dwarf (WD-WD) binaries, with 1.1×10^8 of such systems in our Galaxy. The detached WD-WD binaries evolve by gravitational-radiation reaction and the number of such sources rapidly decreases with increasing orbital frequency. Although it is expected that, above a certain frequency cutoff (1–2 mHz), we will be able to resolve individual signals and remove them from the LISA data, it is still not clear how to further improve the LISA sensitivity to other gravitational wave signals in the region of the frequency band below the WD-WD background frequency cutoff. Although two promising data analysis

*Electronic address: Jeffrey.A.Edlund@jpl.nasa.gov
†Electronic address: Massimo.Tinto@jpl.nasa.gov
‡Also at Institute of Mathematics, Polish Academy of Sciences, Warsaw, Poland.
Electronic address: krolan@aei.mpg.de
§Electronic address: nelemans@astro.ru.nl

procedures have been proposed [5,6] for attempting to subtract the galactic background, considerable work still needs to be done to verify their effectiveness. In this context, simulating the LISA response to the WD-WD background will be particularly useful for verifying present and future data analysis ''cleaning'' algorithms. A realistic simulation will also quantify the effects of the LISA motion around the Sun on the overall amplitude and phase of the GW signal generated by the background in the LISA data. The directional properties of the LISA response and its time dependence introduced by the motion of LISA around the Sun, together with the nonisotropic and nonhomogeneous distribution of the WD-WD binary systems within the galactic disk as seen by LISA, imply that the magnitude of the background observed by LISA will not be a stationary random process. As a consequence of the one-year periodicity of the LISA motion around the Sun, there exist relatively long (≈ 2 months) stretches of data during which the magnitude of the LISA response to the background will reach an absolute minimum [7]. Our simulation shows this minimum to be less than a factor of 2 larger than the level identified by the LISA secondary noises, suggesting the possibility of performing searches for gravitational radiation from other sources located in regions of the sky that are away from the galactic plane. The LISA sensitivity to such signals in fact will be less limited by the WD-WD background during these periods of observation.

This paper is organized as follows. In Sec. II we provide the analytic expression of one of the LISA time-delay interferometric (TDI) responses to a signal radiated by a binary system. Although all the TDI responses to binary signals were first given in their closed analytic form in [8], in what follows we will focus our attention only on the unequal-arm Michelson combination, X. In Sec. III we give a summary of how the WD-WD binary population was obtained, and a description of our numerical simulation of the X response to it. In Sec. IV we describe the numerical implementation of our simulation of the LISA X response to the WD-WD background, and summarize our results. In particular, in agreement with the results by Seto [7], we find the amplitude of the galactic WD-WD background in the LISA X combination to be modulated in time, reaching a minimum when the Sun-LISA direction is roughly oriented towards the Autumn equinox. Furthermore, we show the amplitude of the background at its minimum to be a factor less than 2 larger than the level identified by the LISA noise for a time period of about two months, suggesting that LISA could search (during this time period) for other gravitational wave signals incoming from regions of the sky that are away from the galactic plane.

The time dependence and periodicity of the magnitude of the WD-WD galactic background in the LISA data implies that it is not a stationary but rather a cyclostationary random process of period 1 yr. After providing a brief summary of the theory of cyclostationary random processes relevant to the LISA detection of the WD-WD galactic background, we apply it to three years worth of simulated LISA X data. We find that, by measuring the generalized spectral components of such a cyclostationary random process, LISA will be able to infer key properties of the distribution of the WD-WD binary systems present in our own Galaxy.

II. THE LISA RESPONSE TO SIGNALS FROM BINARY SYSTEMS

The overall LISA geometry is shown in Fig. 1. There are six beams exchanged between the LISA spacecraft, with the six Doppler measurements y_{ij} $(i, j = 1, 2, 3)$ recorded when each received beam is mixed with the laser light of the receiving optical bench. The frequency fluctuations from the six lasers, which enter in each of the six Doppler measurements, need to be suppressed to a level smaller than that identified by the secondary (proof mass and optical path) noises [9] in order to detect and study gravitational radiation at the predicted amplitudes.

Since the LISA triangular array has systematic motions, the two one-way light times between any spacecraft pair are not the same [10]. Delay times for light travel between the spacecraft must be accounted for depending on the sense of light propagation along each link when combining these data as a consequence of the rotation of the array. Following [11], the arms are labeled with single numbers given by the opposite spacecraft; e.g., arm 2 (or $2'$) is opposite spacecraft 2, where primed delays are used to distinguish light times taken in the counterclockwise sense and unprimed delays for the clockwise light times (see Fig. 2). Also the following labeling convention of the Doppler data will be used. Explicitly: y_{23} is the one-way Doppler shift measured at spacecraft 3, coming from spacecraft 2, along arm 1. Similarly, y_{32} is the Doppler shift measured on arrival at spacecraft 2 along arm $1'$ of a signal transmitted from spacecraft 3. Because of the relative motion between spacecraft, $L_1 \neq L_1'$ in general. As in [9,12], we denote six further data streams,

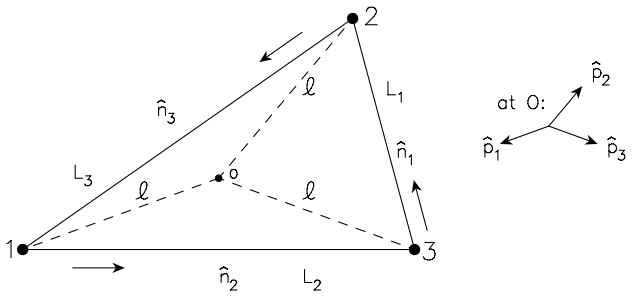

FIG. 1. Schematic LISA configuration. Each spacecraft is equidistant from point o, with unit vectors $\hat{p}_i$ indicating directions to the three spacecraft. Unit vectors $\hat{n}_i$ point between spacecraft pairs with the indicated orientation.

z_{ij} $(i, j = 1, 2, 3)$, as the intraspacecraft metrology data used to monitor the motion of the two optical benches and the relative phase fluctuations of the two lasers on each of the three spacecraft. The frequency fluctuations introduced by the lasers, by the optical benches, by the proof masses, by the fiber optics, and by the measurements themselves at the photodetectors (i.e. the shot-noise fluctuations) enter the Doppler observables y_{ij}, z_{ij} with specific time signatures; see Refs. [9,12] for a detailed discussion. The contribution $y_{ij}^{\rm GW}$ due to GW signals was derived in Ref. [13] in the case of a stationary array, and further extended to the realistic configuration [8] of the LISA array orbiting around the Sun.

Let us consider for instance the "second-generation" unequal-arm Michelson TDI observables, (X_1, X_2, X_3). Their expressions, in terms of the Doppler measurements y_{ij}, z_{ij}, are as follows [14]:

$$X_1 = [(y_{31} + y_{13;2}) + (y_{21} + y_{12;3'})_{;2'2} + (y_{21} + y_{12;3'})_{;33'2'2} + (y_{31} + y_{13;2})_{;33'33'2'2}] - [(y_{21} + y_{12;3'}) + (y_{31} + y_{13;2})_{;33'} + (y_{31} + y_{13;2})_{2'233'} + (y_{21} + y_{12;3'})_{;2'22'233'}] + \tfrac{1}{2}[(z_{21} - z_{31}) - (z_{21} - z_{31})_{;33'} - (z_{21} - z_{31})_{;2'2} + (z_{21} - z_{31})_{;33'33'2'2} + (z_{21} - z_{31})_{;2'22'233'} - (z_{21} - z_{31})_{;2'233'33'2'2}], \quad (1)$$

with X_2, X_3 following from Eq. (1) by permutations of the spacecraft indices. The semicolon notation shown in Eq. (1) emphasizes that the operation of sequentially applying two or more delays to a given measurement is noncommutative as consequence of the time dependence of the light times L_i and L_i' $(i = 1, 2, 3)$, and a specific order has to be adopted to adequately suppress the laser noises [11,14,15]. Specifically: $y_{ij;kl} \equiv y_{ij}(t - L_l(t) - L_k(t - L_l)) \neq y_{ij;lk}$ (units in which the speed of light $c = 1$).

The expressions of the gravitational wave signal and the secondary noise sources entering into X_1 will in general be different from those entering into X, the corresponding "-first-generation" unequal-arm Michelson observable derived under the assumption of a stationary LISA array [12,13]. However, the magnitude of the corrections introduced by the motion of the array is proportional to the product between the time derivative of the GW amplitude and the difference between the actual light travel times and those valid for a stationary array. At 1 Hz, for instance, the larger correction to the signal (due to the difference between the corotating and counterrotating light travel times) is 2 orders of magnitude smaller than the main signal. Since the amplitude of this correction scales linearly with the Fourier frequency, we can completely disregard this effect (and the weaker effect due to the time dependence of the light travel times) over the entire LISA band [11]. Furthermore, since along the LISA orbit the three armlengths will differ at most by $\sim$1%–2%, the degradation in signal-to-noise ratio introduced by adopting signal templates that neglect the inequality of the armlengths will be of only a few percent. For these reasons, in what follows we will focus on the expressions of the GW responses of various second-generation TDI observables by disregarding the differences in the delay times experienced by light propagating clockwise and counterclockwise, and by assuming the three LISA armlengths to be constant and equal to $L = 5 \times 10^6$ km $\simeq 16.67$ s [1]. These approximations, together with the treatment of the moving-LISA GW response discussed in [8] are essentially equivalent to the *rigid adiabatic approximation* of Ref. [16], and to the formalism of Ref. [7].

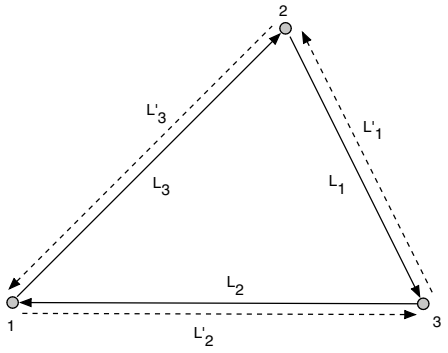

FIG. 2. Schematic diagram of LISA configurations involving six laser beams. Optical path delays taken in the counterclockwise sense are denoted with a prime, while unprimed delays are in the clockwise sense.

These considerations imply that the second-generation TDI expressions for the gravitational wave signal and the secondary noises can be expressed in terms of the corresponding first-generation TDIs. For instance, the gravitational wave signal entering into the second-generation unequal-arm Michelson combination, $X_1^{\rm GW}$, can be written in terms of the gravitational wave response of the corresponding first-generation unequal-arm Michelson combination, $X^{\rm GW}(t)$, in the following manner [17]:

$$X_1^{\rm GW}(t) = X^{\rm GW}(t) - X^{\rm GW}(t - 4L). \quad (2)$$

Equation (2) implies that any data analysis procedure and algorithm that will be implemented for the second-generation TDI combinations can actually be derived by considering the corresponding first-generation TDI expressions. For this reason, from now on we will focus our attention on the gravitational wave responses of the first-generation combinations.

The gravitational wave response $X^{\rm GW}(t)$ of the unequal-arm Michelson TDI combination to a signal from a binary system has been derived in [8], and it can be written in the

following form:

$$X^{\rm GW}(t) = \Re[A(x,t)e^{-i\phi(t)}], \tag{3}$$

where $x = \omega_s L$ (ω_s being the angular frequency of the GW signal in the source reference frame), and the expressions for the complex amplitude $A(x,t)$ and the real phase $\phi(t)$ are

$$\begin{aligned} A(x,t) = 2x\sin(x)\Bigg\{&\Bigg[\,\mathrm{sinc}\Bigg[(1+c_2(t))\frac{x}{2}\Bigg]e^{ix[(3/2)+d_2(t)]} \\ &+ \mathrm{sinc}\Bigg[(1-c_2(t))\frac{x}{2}\Bigg]e^{ix[(5/2)+d_2(t)]}\Bigg]\mathcal{B}_2(t) \\ &-\Bigg[\,\mathrm{sinc}\Bigg[(1-c_3(t))\frac{x}{2}\Bigg]e^{ix[(3/2)+d_3(t)]} \\ &+ \mathrm{sinc}\Bigg[(1+c_3(t))\frac{x}{2}\Bigg]e^{ix[(5/2)+d_3(t)]}\Bigg]\mathcal{B}_3(t)\Bigg\}, \end{aligned} \tag{4}$$

$$\phi(t) = \omega_s t + \omega_s R\cos\beta\cos(\omega_s t + \eta_0 - \lambda). \tag{5}$$

In Eq. (5) R is the distance of the guiding center of the LISA array, o, from the solar system barycenter, (β, λ) are the ecliptic latitude and longitude, respectively, of the source location in the sky, $\Omega = 2\pi/\mathrm{yr}$, and η_0 defines the position of the LISA guiding center in the ecliptic plane at time $t = 0$. Note that the functions $c_k(t)$, $d_k(t)$, and $\mathcal{B}_k(t)$ $(k = 2, 3)$ do not depend on x. The analytic expressions for $c_k(t)$, and $d_k(t)$ are the same as those given in Eqs. (46) and (47) of Ref. [8], while the functions $\mathcal{B}_k(t)$ $(k = 2, 3)$ are equal to

$$\mathcal{B}_k(t) = (a^{(1)} + ia^{(3)})u_k(t) + (a^{(2)} + ia^{(4)})v_k(t). \tag{6}$$

The coefficients $(a^{(1)}, a^{(2)}, a^{(3)}, a^{(4)})$ depend only on the two independent amplitudes of the gravitational wave signal, $(h_+, h_\times)$, the polarization angle, ψ, and an arbitrary phase, ϕ_0, that the signal has at time $t = 0$. Their analytic expressions are given in Eqs. (41)–(44) of Ref. [8], while the functions $u_k(t)$, and $v_k(t)$ $(k = 2, 3)$ are given in Eqs. (27) and (28) in the same reference.

Since most of the gravitational wave energy radiated by the galactic WD-WD binaries will be present in the lower part of the LISA sensitivity frequency band, say between 10^{-4}–10^{-3} Hz, it is useful to provide an expression for the Taylor expansion of the X response in the long-wavelength limit (LWL), i.e. when the wavelength of the gravitational wave signal is much larger than the LISA armlength ($x \ll 1$). As it will be shown in the following sections, the LWL expression will allow us to analytically describe the general features of the white-dwarf background in the X combination, and derive computationally efficient algorithms for numerically simulating the WD-WD background in the LISA data.

The nth-order truncation, $X^{\rm GW}_{(n)}(t)$, of the Taylor expansion of $X^{\rm GW}(t)$ in power series of x can be written in the following form:

$$X^{\rm GW}_{(n)}(t) = \mathrm{Re}\sum_{k=0}^{n} A^{(k)}(t)x^{k+2}e^{-i\phi(t)}, \tag{7}$$

where the first three functions of time $A^{(k)}(t)$, $k \le 2$ are equal to

$$\begin{aligned} A^{(0)} &= 4[\mathcal{B}_2 - \mathcal{B}_3], \\ A^{(1)} &= 4i[(d_2+2)\mathcal{B}_2 - (d_3+2)\mathcal{B}_3], \\ A^{(2)} &= \Bigg[2d_3^2 + 8d_3 + \frac{28}{3} + \frac{1}{6}c_3^2\Bigg]\mathcal{B}_3 \\ &\quad - \Bigg[2d_2^2 + 8d_2 + \frac{28}{3} + \frac{1}{6}c_2^2\Bigg]\mathcal{B}_2. \end{aligned} \tag{8}$$

Note that the form we adopted for $X^{\rm GW}(t)$ [Eq. (3)] makes the derivation of the functions $A^{(k)}(t)$ particularly easy since the dependence on x in $A(x,t)$ is now limited only to the coefficients in front of the two functions $\mathcal{B}_2(t)$ and $\mathcal{B}_3(t)$ [see Eq. (4)].

Although it is generally believed that the lowest order long-wavelength expansion of the X combination, $X^{\rm GW}_{(0)}$, is sufficiently accurate in representing a gravitational wave signal in the low part of the LISA frequency band, there has not been in the literature any quantitative analysis of the error introduced by relying on such a zero-order approximation. Since any TDI combination will contain a linear superposition of tens of millions of signals, it is crucial to estimate such an error as a function of the order of the approximation, n. In order to determine how many terms we need to use for a given signal angular frequency, ω_s, we will rely on the following "matching function":

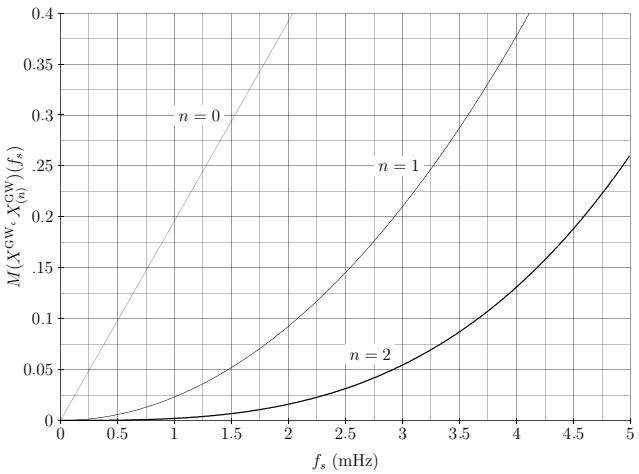

FIG. 3. Plots of the percentage root-mean-squared errors, $M(X^{\rm GW}, X^{\rm GW}_{(n)})$, associated with the long-wavelength expansion index n, as functions of the gravitational wave frequency, f_s. The source location has been assumed to be in the center of our Galaxy.

$$M(X^{\rm GW}, X^{\rm GW}_{(n)}) \equiv \sqrt{\frac{\int_0^T [X^{\rm GW}(t) - X^{\rm GW}_{(n)}(t)]^2 dt}{\int_0^T [X^{\rm GW}(t)]^2 dt}}. \quad (9)$$

Equation (9) estimates the percent root-mean-squared error implied by using the nth order LWL approximation. In Fig. 3 we plot M as a function of the signal frequency, f_s ($= \omega_s/2\pi$), for $n = 0, 1, 2$. At 5×10^{-4} Hz, for instance, the zero-order LWL approximation ($n = 0$) of the X combination shows an rms deviation from the exact response equal to about 10%. As expected, this inaccuracy increases for signals of higher frequencies, becoming equal to 40% at 2×10^{-3} Hz. With $n = 1$ the accuracy improves showing that the $X^{\rm GW}_{(1)}$ response deviates from the exact one with an rms error smaller than 10% in the frequency band $(10^{-4}$–$2 \times 10^{-3})$ Hz. In our simulation we have actually implemented the $n = 2$ LWL expansion because it was possible and easy to do.

III. WHITE-DWARF BINARY POPULATION DISTRIBUTION

The gravitational wave signal radiated by a WD-WD binary system depends on eight parameters, $(\phi_o, \iota, \psi, D, \beta, \lambda, \mathcal{M}_c, \omega_s)$, which are the constant phase of the signal (ϕ_o) at the starting time of the observation, the inclination angle (ι) of the angular momentum of the binary system relative to the line of sight, the polarization angle (ψ) describing the orientation of the wave polarization axes, the distance (D) to the binary, the angles (λ, β) describing the location of the source in the sky relative to the ecliptic plane, the chirp mass ($\mathcal{M}_c$), and the angular frequency (ω_s) in the source reference frame, respectively. Since it can safely be assumed that the chirp mass $\mathcal{M}_c$ and the angular frequency ω_s are independent of the source location [2] and of the remaining angular parameters ϕ_o, ι, ψ, and because there are no physical arguments for preferred values of the constant phase ϕ_o and the orientation of the binary given by the angles ι and ψ, it follows that the joint probability distribution, $P(\phi_o, \iota, \psi, D, \beta, \lambda, \mathcal{M}_c, \omega_s)$, can be rewritten in the following form:

$$P(\phi_o, \iota, \psi, D, \beta, \lambda, \mathcal{M}_c, \omega_s) = P_1(\phi_o) P_2(\iota) P_3(\psi) P_4(D, \beta, \lambda) P_5(\mathcal{M}_c, \omega_s). \quad (10)$$

In the implementation of our simulation we have assumed the angles ϕ_o and ψ to be uniformly distributed in the interval $[0, 2\pi)$, and $\cos\iota$ uniformly distributed in the interval $[-1, 1]$. We further assumed the binary systems to be randomly distributed in the galactic disc according to the following axially symmetric distribution $\mathcal{P}_4(\mathcal{R}, z)$ [see [2] Eq. (5)]:

$$\mathcal{P}_4(\mathcal{R}, z) = \frac{e^{-R/H} \, {\rm sech}^2(z/z_o)}{4\pi z_o H^2}, \quad (11)$$

where $(\mathcal{R}, z)$ are cylindrical coordinates with origin at the galactic center, $H = 2.5$ kpc, and $z_o = 200$ pc, and it is proportional to $P_4(D, \lambda, \beta)$ through the Jacobian of the coordinate transformation. Note that the position of the Sun in this coordinate system is given by $\mathcal{R}_\odot = 8.5$ kpc and $z_\odot = -30$ pc. We then generate the positions of the sources from the distribution given by Eq. (11) and map them to their corresponding ecliptic coordinates (D, β, λ).

The physical properties of the WD-WD population [$\mathcal{M}_c \equiv (m_1 m_2)^{3/5}/(m_1 + m_2)^{1/5}$, with m_1, m_2 being the masses of the two stars, and $\omega_s = 2\pi f_s = 4\pi/$orbital period] are taken from the binary population synthesis simulation discussed in [18]. For details on this simulation we refer the reader to [18], and for earlier work to [2–4,19–21]. The basic ingredient for these simulations is an approximate binary evolution code. A representation of the complete galactic population of binaries is produced by evolving a large (typically 10^6) number of binaries from their formation to the current time, where the distributions of the masses and separations of the initial binaries are estimated from the observed properties of local binaries. This initial-to-final parameter mapping is then convolved with an estimate of the binary formation rate in the history of the Galaxy to obtain the total galactic population of binaries at the present time. From these the binaries of interest can then be selected. In principle this technique is very powerful, although the results can be limited by the limited knowledge we have on many aspects of binary evolution. For WD-WD binaries, the situation is better than for many other populations, since the observed population of WD-WD binaries allows us to gauge the models (e.g. [2]).

We also include the population of semidetached WD-WD binaries (usually referred to as AM CVn systems) that are discussed in detail in [18]. In these binaries one white dwarf transfers its outer layers onto a companion white dwarf. Because of the redistribution of mass in the system, the orbital period of these binaries increases in time, even though the angular momentum of the binary orbit still decreases due to gravitational wave losses. The formation of these systems is very uncertain, mainly due to questions concerning the stability of the mass transfer (e.g. [22]).

From the models of the galactic population of the detached WD-WD binaries and AM CVn systems two dimensional histograms were created, giving the expected number of both detached WD-WD binaries and AM CVn systems currently present in the Galaxy as a function of the log of the GW radiation frequency, $f_s (= \omega_s/2\pi)$ and chirp mass, $\mathcal{M}_c$. In the case of the detached WD-WD binaries, the $(\log f_s, \mathcal{M}_c)$ space was defined over the set $\mathcal{M}_c \in (0, 1.5]$, $\log f_s \in [-6, -1]$, and contained 30×50 grid points, while in the case of the AM CVn systems the region

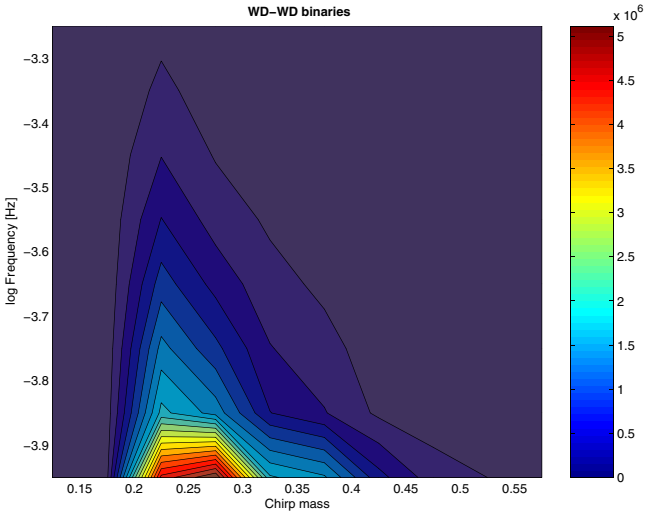

FIG. 4 (color online). The distribution of detached white-dwarf–white-dwarf binaries in our Galaxy as a function of the gravitational wave frequency, f_s, and chirp mass, $\mathcal{M}_c$.

is intrinsically smaller, $\mathcal{M}_c \in (0, 1.2]$, $\log f_s \in [-4, -1.5]$, containing only 24×25 grid points.

Figure 4 shows the distribution of the number of detached WD-WD binaries as a function of the chirp mass and signal frequency in the form of a contour plot. This distribution reaches its maximum within the LISA frequency band when the chirp mass is equal to $\simeq 0.25\mathcal{M}_\odot$, and it monotonically decreases as a function of the signal frequency. The distribution of the number of AM CVn systems has instead a rather different shape, as shown by the contour plot given in Fig. 5. The region of the $(\mathcal{M}_c, \log f_s)$ space over which the distribution is nonzero

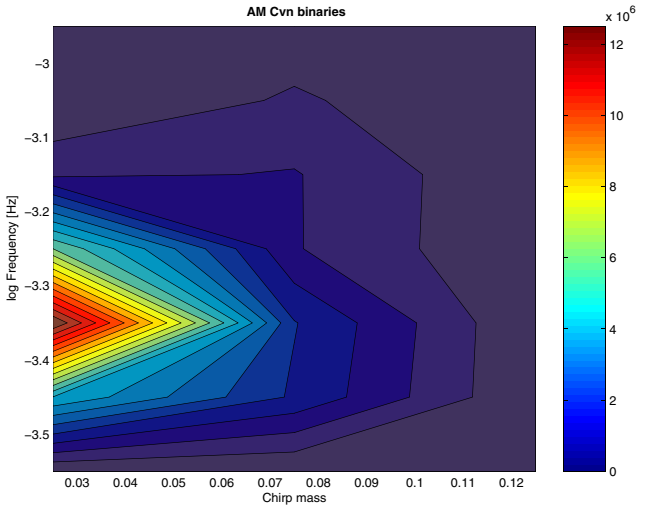

FIG. 5 (color online). The distribution of AM CVn binary systems in our Galaxy as a function of the gravitational wave frequency, f_s, and chirp mass, $\mathcal{M}_c$.

is equal to $(0, 0.07) \times (-3.4, -2.2)$, and it reaches its maximum at the point $(0.03, -3.35)$.

IV. SIMULATION OF THE BACKGROUND SIGNAL IN THE LISA DATA

In order to simulate the LISA X response to the population of WD-WD binaries derived in Sec. III one needs to coherently add the LISA response to each individual signal. Although this could naturally be done in the time domain, the actual CPU time required to successfully perform such a simulation would be unacceptably long. The generation in the time domain of 1 yr of $X^{\rm GW}(t)$ response to a single signal sampled at a rate of 16 s would require about 1 s with an optimized C ++ code running on a Pentium IV 3.2 GHz processor. Since the number of signals from the background is of the order 10^8, it is clear that a different algorithm is needed for simulating the background in the LISA data within a reasonable amount of time. We were able to derive and implement numerically an analytic formula of the Fourier transform of each binary signal, which has allowed us to reduce the computational time by almost a factor 100. Furthermore, we have run our code on the Jet Propulsion Laboratory supercomputer system, which includes 64 Intel Itanium2 processors each with a clock speed of 900 MHz.

A. The Fourier transform of a binary signal

The expression of the Fourier transform of the TDI response $X^{\rm GW}$ to a single binary signal [Eqs. (3)–(5)] cannot be written (to our knowledge) in closed analytic form. However, by using the LWL expansion of the $X^{\rm GW}$ response, it is possible to obtain a closed-form expression of its Fourier transform. Since the WD-WD binary background has a natural frequency cutoff that is between 1 and 2 mHz [3,18], the LWL expansion of the $X^{\rm GW}$ response [Eq. (7)], truncated at $n = 2$, can be used for accurately representing the gravitational wave response of each binary signal, as discussed in Sec. II.

In order to derive the Fourier transform of $X^{\rm GW}_{(2)}(t)$, we use the following expansion of the function $e^{-i\phi(t)}$ in terms of the Bessel functions of the first kind, J_q [23]:

$$e^{-i\phi(t)} = \sum_{q=-\infty}^{\infty} J_q(\omega_s R\cos\beta) e^{-i\{\omega_s t + q[\Omega t + \eta_0 - \lambda + (\pi/2)]\}}. \tag{12}$$

Since the Bessel functions $|J_q(\omega_s R\cos\beta)|$ are much smaller than unity when $|q| \gg |\omega_s R\cos\beta|$, the expansion given by Eq. (12) can be truncated at a finite index Q, providing an accurate numerical estimation of the function $e^{-i\phi(t)}$. These considerations allow us to write the following expression of the Fourier transform of $X^{\rm GW}_{(n)}(t)$:

$$\tilde{X}^{\mathrm{GW}}_{(n)}(\omega) = \mathcal{F}\left(\Re \sum_{k=0}^{n} \sum_{q=-Q}^{Q} A^{(k)}(t) x^{k+2} J_q(\omega_s R\cos\beta) e^{-i\{\omega_s t + q[\Omega t + \eta_0 - \lambda + (\pi/2)]\}}\right)$$

$$= \pi \sum_{q=-Q}^{Q} J_q(\omega_s R\cos\beta) \sum_{k=0}^{n} x^{k+2} \{\mathcal{F}(\Re[A^{(k)}(t)]) * [\delta(\omega + \omega_s + q\Omega) e^{iq(-\eta_0+\lambda-\pi/2)} + \delta(-\omega + \omega_s + q\Omega)$$
$$\times e^{iq(\eta_0-\lambda+\pi/2)}] + i\mathcal{F}(\Im[A^{(k)}(t)]) * [\delta(\omega + \omega_s + q\Omega) e^{iq(-\eta_0+\lambda-\pi/2)} - \delta(-\omega + \omega_s + q\Omega) e^{iq(\eta_0-\lambda+\pi/2)}]\}, \quad (13)$$

where $\mathcal{F}$ is the Fourier transform operator, the symbol $*$ between two expressions means their convolution, ω is the Fourier angular frequency, and $A^{(k)}(t)$ are defined in Eq. (7) and given in Eq. (8) with $k = 0, 1, 2$.

As an example application of this general formula for the Fourier transform of the $X^{\mathrm{GW}}_{(n)}(t)$ response, let us apply it to the lowest order LWL expansion ($n = 0$)

$$\tilde{X}^{\mathrm{GW}}_{(0)}(\omega) = 4\pi \sum_{q=-Q}^{Q} J_q(\omega_s R\cos\beta) x^2 \{[a_1(\tilde{u}_2(\omega) - \tilde{u}_3(\omega)) + a_2(\tilde{v}_2(\omega) - \tilde{v}_3(\omega))] * [\delta(\omega + \omega_s + q\Omega) e^{iq(-\eta_0+\lambda-\pi/2)}$$
$$+ \delta(-\omega + \omega_s + q\Omega) e^{iq(\eta_0-\lambda+\pi/2)}] + i[a_3(\tilde{u}_2(\omega) - \tilde{u}_3(\omega)) + a_4(\tilde{v}_2(\omega) - \tilde{v}_3(\omega))]$$
$$* [\delta(\omega + \omega_s + q\Omega) e^{iq(-\eta_0+\lambda-\pi/2)} - \delta(-\omega + \omega_s + q\Omega) e^{iq(\eta_0-\lambda+\pi/2)}]\}. \quad (14)$$

Since the Fourier transforms of u and v are both linear combinations of nine Dirac delta functions centered on the frequencies $\pm l\Omega$, $l = 0, 1, 2, 3, 4$ [see Eqs. (27)–(30) in Ref. [8] for the expressions of u and v], it follows that $\tilde{X}^{\mathrm{GW}}_{(0)}(\omega)$ is also a linear combination of Dirac delta functions. In particular, in the limit of negligible Doppler modulation, the resulting expression (14) reduces as expected to that of a purely amplitude modulated sinusoidal signal with central frequency equal to ω_s and upper and lower bandlimits given by $\omega_s + 4\Omega$ and $\omega_s - 4\Omega$, respectively [24].

The actual expression of the Fourier transform we implemented in our simulation of the WD-WD background used Eq. (13) with $n = 2$, and maximum value of the index of the Bessel expansion, Q, equal to $|\omega_s R\cos\beta| + 20$ in order to make negligible the error associated with the truncation of the expansion itself.

One extra mathematical detail that we need to include is that the Fourier transform of $X^{\mathrm{GW}}_{(n)}(t)$ is performed over a finite integration time, T, while the expression in Eq. (13) corresponds to an infinite-time Fourier transform. In order to account for this discrepancy we convolved the analytic Fourier transform of the signal given in Eq. (13) with the Fourier transform of a window function with an integration time T. To avoid leakage introduced by using a simple rectangular window, we have used instead Nuttall's modified Blackman-Harris window [25]. Although this window is characterized by having the main lobe of its Fourier transform slightly wider than that of the rectangular window, the maximum of its sidelobes are about 4 orders of magnitude lower than those of the rectangular window, reducing leakage significantly. The expression of its Fourier transform, $\tilde{W}(\omega)$, is equal to

$$\tilde{W}(\omega) = n_0[\mathrm{Sinc}(\omega T) + i\,\mathrm{Cosc}(\omega T)] - n_1[\mathrm{Sinc}(\omega T + 2\pi) + \mathrm{Sinc}(\omega T - 2\pi) + i(\mathrm{Cosc}(\omega T + 2\pi) + \mathrm{Cosc}(\omega T - 2\pi))]$$
$$- n_2[\mathrm{Sinc}(\omega T + 4\pi) + \mathrm{Sinc}(\omega T - 4\pi) + i(\mathrm{Cosc}(\omega T + 4\pi) + \mathrm{Cosc}(\omega T - 4\pi))] - n_3[\mathrm{Sinc}(\omega T + 6\pi)$$
$$+ \mathrm{Sinc}(\omega T - 6\pi) + i(\mathrm{Cosc}(\omega T + 6\pi) + \mathrm{Cosc}(\omega T - 6\pi))], \quad (15)$$

where the functions Sinc(.) and Cosc(.) are defined as follows:

$$\mathrm{Sinc}\,(.) \equiv \frac{\sin(.)}{.}, \qquad \mathrm{Cosc}(.) \equiv \frac{\cos(.) - 1}{.}, \quad (16)$$

and the coefficients n_r, $r = 0, 1, 2, 3$ have the following numerical values:

$$n_0 = 0.363\,581\,9, \qquad n_1 = 0.244\,588\,75,$$
$$n_2 = 0.068\,299\,75, \qquad n_3 = 0.005\,320\,55. \quad (17)$$

B. Generation of the signal parameters

We used the distributions given in Sec. III to randomly generate the parameters ϕ_o, ι, ψ, D, β, λ, while the values of the chirp mass, $\mathcal{M}_c$, and the logarithm of the frequency of the signal, $\log(f_s)$, were obtained by further processing the numeric distribution function (given in Sec. III) of the number of sources. To derive the distribution function for the variables $(\mathcal{M}_c, \log(f_s))$ within each grid rectangle of our numerical distribution we proceeded in the following way [26]. Let us consider the number of sources $N(x_1, x_2)$ as a function of two coordinates (x_1, x_2) of a point in the $(\mathcal{M}_c, \log(f_s))$ plane within a specified grid rectangle of the numerical distribution. This function can be approximated there by the following quadratic polynomial:

$$N(x_1, x_2) = n_{00}(1 - x_1)(1 - x_2) + n_{11}x_1x_2 + n_{01}(1 - x_1)x_2 + n_{10}x_1(1 - x_2), \quad (18)$$

where n_{00}, n_{11}, n_{01}, n_{10} are equal to the number of signals at the ''corners'' of the considered grid rectangle and are obtained by interpolation; (x_1, x_2) are therefore two real numbers defined in the range $[0, 1]$.

If we integrate out the x_2 dependence in $N(x_1, x_2)$ we obtain

$$N_{x_2}(x_1) = \int_0^1 N(x_1, x_2)dx_2 = \frac{(-n_{00} + n_{11} - n_{01} + n_{10})x_1 + n_{00} + n_{01}}{2}, \tag{19}$$

which defines the total number of sources within that grid rectangle having chirp mass equal to x_1. In order to derive the probability distribution function of x_1 within that grid rectangle we can define the following mapping between a uniformly distributed random variable, say z_1, and the random variable x_1:

$$z_1 = \frac{\int_0^{x_1} N_{x_2}(x_1')dx_1'}{\int_0^1 N_{x_2}(x_1')dx_1'} = \frac{(-n_{00} + n_{11} - n_{01} + n_{10})x_1^2 + 2(n_{00} + n_{01})x_1}{n_{00} + n_{11} + n_{01} + n_{10}}. \tag{20}$$

By solving the above nonlinear equation for every uniformly sampled z_1 we obtain

$$x_1 = \frac{n_{00} + n_{01} - \sqrt{n_{00}^2 + 2n_{00}n_{01} + n_{01}^2 + (-n_{00}^2 - 2n_{00}n_{01} + n_{11}^2 + 2n_{11}n_{10} - n_{01}^2 + n_{10}^2)z_1}}{n_{00} - n_{11} + n_{01} - n_{10}}, \tag{21}$$

where the branch ''$-$'' has been chosen such that x_1 remains in the range $[0, 1]$. If $n_{00} - n_{11} + n_{01} - n_{10} = 0$ then Eq. (21) is no longer valid, and we have instead $x_1 = z_1$.

A similar procedure can be implemented for calculating x_2. By integrating $N(x_1, x_2')$ with respect to x_2' over the range $(0, x_2)$, we can establish the following relationship between another uniformly distributed random variable, say z_2, and x_2:

$$z_2 = \frac{\int_0^{x_2} N(x_1, x_2')dx_2'}{\int_0^1 N(x_1, x_2')dx_2'} = \frac{[(n_{00} + n_{11} - n_{01} - n_{10})x_1 - n_{00} + n_{01}]x_2^2 + 2[(-n_{00} + n_{10})x_1 + n_{00}]x_2}{(-n_{00} + n_{11} - n_{01} + n_{10})x_1 + n_{00} + n_{01}}. \tag{22}$$

After some simple algebra we can finally solve for x_2 in terms of x_1 (itself a function of the uniformly distributed random variable z_1) and z_2

$$x_2 = \frac{n_{00}(x_1 - 1) - n_{10}x_1 + \sqrt{F(x_1)z_2 + (n_{00}^2 - 2n_{00}n_{10} + n_{10}^2)x_1^2 + 2(-n_{00}^2 + n_{00}n_{10})x_1 + n_{00}^2}}{(n_{11} - n_{01} - n_{10} + n_{00})x_1 - n_{00} + n_{01}}, \tag{23}$$

where now we have chosen the ''$+$'' branch so $x_2 \in [0, 1]$ range, and the function $F(x_1)$ is equal to

$$F(x_1) \equiv (n_{11}^2 + n_{01}^2 - n_{00}^2 - 2n_{01}n_{11} + 2n_{00}n_{10} - n_{10}^2)x_1^2 + 2(-n_{00}n_{10} + n_{00}^2 - n_{01}^2 + n_{01}n_{11})x_1 - n_{00}^2 + n_{01}^2. \tag{24}$$

Note that the equation for x_2 above is no longer valid when $(n_{11} - n_{01} - n_{10} + n_{00})x_1 - n_{00} + n_{01} = 0$, in which case $x_2 = z_2$. Once x_1 and x_2 are calculated, they can be converted into the physical parameters $\mathcal{M}_c$ and ω_s according to the following relationships:

$$\mathcal{M}_c = \mathcal{M}_{c00} + x_1\Delta_{\mathcal{M}_c} \tag{25}$$

$$\omega_s = 2\pi 10^{\log(f_{s00}) + x_2\Delta_{\log(f_s)}} \tag{26}$$

where $(\mathcal{M}_{c00}, \log(f_{s00}))$ are the coordinates of the ''lower-left-hand corner'' of the considered grid rectangle, and $\Delta_{\mathcal{M}_c}$, $\Delta_{\log(f_s)}$ are the lengths of the sides of the grid rectangle.

C. Results of the numerical simulation

The expression for the finite-time Fourier transform of each WD-WD signal in the $\tilde{X}^{\mathrm{GW}}$ response given in Sec. IV A allows us to coherently add in the Fourier domain all the signals radiated by the WD-WD galactic binary population described in Sec. III. After inverse Fourier transforming the synthesized response and removing the window from it, we finally obtain the time-domain representation of the background as it will be seen in the LISA TDI combination X. This is shown in Fig. 6, where we plot three years worth of simulated $X^{\mathrm{GW}}(t)$, and include the LISA noise [1]. The one-year periodicity induced by the motion of LISA around the Sun is clearly noticeable. One other interesting feature shown by Fig. 6 is that the amplitude response reaches absolute minima when the Sun-LISA direction is roughly oriented towards the Autumn equinox, while the absolute maxima take place when the Sun-LISA direction is oriented roughly towards the galactic center [7]. This fact can easily be understood by looking at Fig. 7. Since the ecliptic plane is not parallel to the galactic plane, and because our own solar system is about 8.5 kpc away from the galactic center (where most of the

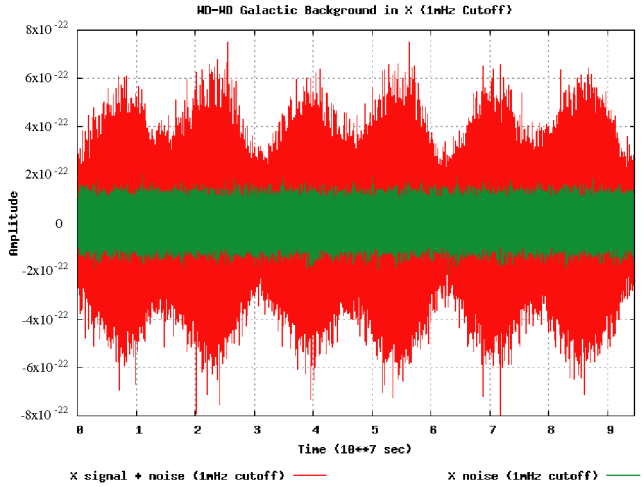

FIG. 6 (color online). Three years of simulated TDI X response to the WD-WD galactic background signal. The time series of the LISA instrumental noise is displayed for comparison.

WD-WD binaries are concentrated) it follows that the LISA X^{GW} response does not have a six-month periodicity.

Note also that, for a time period of about 2 months, the absolute minima reached by the amplitude of the LISA response to the WD-WD background is only a factor less than 2 larger than the level of the instrumental noise. This implies that during these observation times LISA should be able to search for other sources of gravitational radiation that are not located in the galactic plane. This might turn out to be the easiest way to mitigate the detrimental effects of the WD-WD background when searching for other sources of gravitational radiation. We will quantitatively analyze in a follow-up work how to take advantage of this observation in order to optimally search, during these time periods, for sources that are off the galactic plane.

In Fig. 8 we plot, as functions of the Fourier frequency, f, the windowed Fourier powers of both the signal and the noise entering into the TDI X combination. Note that in the region of the LISA band below 0.2 mHz the power of the

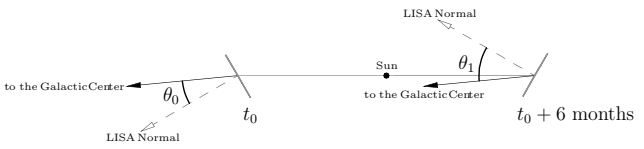

FIG. 7. Two snapshots of LISA along its trajectory as recorded six months apart by an observer in the ecliptic plane. They correspond to the times when the LISA response to the background achieves a local maximum. The magnitudes of these maxima are not equal due to the relative disposition of the ecliptic plane with respect to the galactic plane. At time t_0 the angle θ_0 between the normal to the plane of LISA and a vector pointing to the galactic center is equal to 24.47°. Six months later, when the LISA response is also at a maximum, the angle θ_1 is equal to 35.53° which results in a smaller maximum.

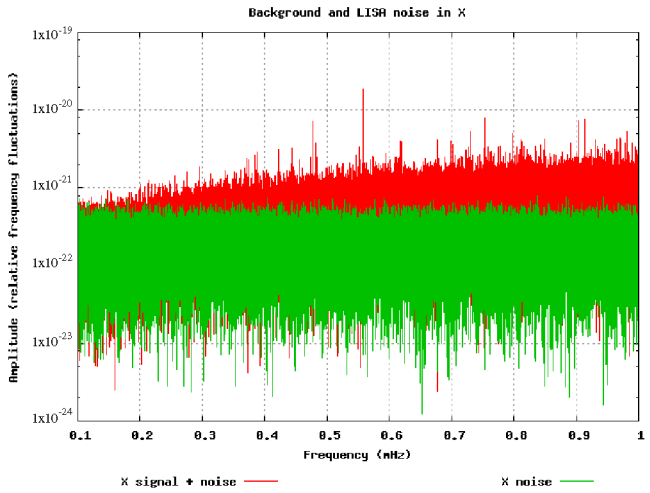

FIG. 8 (color online). The amplitude of the Fourier transform of the WD-WD galactic background gravitational wave signal and of the LISA instrumental noise entering into the TDI combination X.

WD-WD background is smaller than that of the instrumental noise.

V. CYCLOSTATIONARY PROCESSES

The results of our simulation (Fig. 6) indicate that the LISA X^{GW} response to the background can be regarded, in a statistical sense, as a periodic function of time. This is a consequence of the deterministic (and periodic) motion of the LISA array around the Sun. Since its autocorrelation function will also be a periodic function of period 1 yr, it follows that any LISA response to the WD-WD background should no longer be treated as a stationary random process but rather as a periodically correlated random process. These kind of processes have been studied for many years, and are usually referred to as cyclostationary random processes (see [27] for a comprehensive overview of the subject and for more references). In what follows we will briefly summarize the properties of cyclostationary processes that are relevant to our problem.

A continuous stochastic process $\mathcal{X}(t)$ having finite second order moments is said to be *cyclostationary* with period T if the following expectation values:

$$E[\mathcal{X}(t)] = m(t) = m(t+T), \tag{27}$$

$$E[\mathcal{X}(t')\mathcal{X}(t)] = C(t', t) = C(t'+T, t+T) \tag{28}$$

are periodic functions of period T, for every $(t', t) \in \mathbf{R} \times \mathbf{R}$. For simplicity from now on we will assume $m(t) = 0$.

If $\mathcal{X}(t)$ is cyclostationary, then the function $B(t, \tau) \equiv C(t+\tau, t)$ for a given $\tau \in \mathbf{R}$ is periodic with period T, and it can be represented by the following Fourier series:

$$B(t, \tau) = \sum_{r=-\infty}^{\infty} B_r(\tau) e^{i2\pi(rt/T)}, \tag{29}$$

where the functions $B_r(\tau)$ are given by

$$B_r(\tau) = \frac{1}{T}\int_0^T B(t,\tau)e^{-i2\pi r(t/T)}dt. \quad (30)$$

The Fourier transforms $g_r(f)$ of $B_r(\tau)$ are the so-called ''cyclic spectra'' of the cyclostationary process $\mathcal{X}(t)$ [27]

$$g_r(f) = \int_{-\infty}^{\infty} B_r(\tau)e^{-i2\pi f\tau}d\tau. \quad (31)$$

If a cyclostationary process is real, the following relationships between the cyclic spectra hold:

$$B_{-r}(\tau) = B_r^*(\tau), \quad (32)$$

$$g_{-r}(-f) = g_r^*(f), \quad (33)$$

where the symbol $*$ means complex conjugation. This implies that, for a real cyclostationary process, the cyclic spectra with $r \geq 0$ contain all the information needed to characterize the process itself.

The function $\sigma^2(\tau) \equiv B(0,\tau)$ is the variance of the cyclostationary process $\mathcal{X}(t)$, and it can be written as a Fourier decomposition as a consequence of Eq. (30)

$$\sigma^2(\tau) = \sum_{r=-\infty}^{\infty} H_r e^{i2\pi(r\tau/T)}, \quad (34)$$

where $H_r \equiv B_r(0)$ are harmonics of the variance σ^2. From Eq. (32) it follows that $H_{-r} = H_r^*$.

For a discrete, finite, real time series $\mathcal{X}_t$, $t = 1, \ldots, \mathcal{N}$ we can estimate the cyclic spectra by generalizing standard methods of spectrum estimation used with stationary processes. Assuming again the mean value of the time series $\mathcal{X}_t$ to be zero, the cyclic autocorrelation sequences are defined as

$$s_l^r = \frac{1}{\mathcal{N}}\sum_{t=1}^{\mathcal{N}-|l|} \mathcal{X}_t\mathcal{X}_{t+|l|}e^{-\{[i2\pi r(t-1)]/T\}}. \quad (35)$$

It has been shown [27] that the cyclic autocorrelations are asymptotically (i.e. for $N \rightarrow \infty$) unbiased estimators of the functions $B_r(\tau)$. The Fourier transforms of the cyclic autocorrelation sequences s_l^r are estimators of the cyclic spectra $g_r(f)$. These estimators are asymptotically unbiased, and are called ''inconsistent estimators'' of the cyclic spectra, i.e. their variances do not tend to zero asymptotically. In the case of Gaussian processes [27] consistent estimators can be obtained by first applying a lag window to the cyclic autocorrelation and then perform a Fourier transform. This procedure represents a generalization of the well-known technique for estimating the spectra of stationary random processes [28].

An alternative procedure for identifying consistent estimators of the cyclic spectra is to first take the Fourier transform, $\tilde{\mathcal{X}}(f)$, of the time series $\mathcal{X}(t)$

$$\tilde{\mathcal{X}}(f) = \sum_{t=1}^{\mathcal{N}} \mathcal{X}_t e^{-i2\pi f(t-1)} \quad (36)$$

and then estimate the cyclic periodograms $g_r(f)$

$$g_r(f) = \frac{\tilde{\mathcal{X}}(f)\tilde{\mathcal{X}}^*(f - \frac{2\pi r}{T})}{\mathcal{N}}. \quad (37)$$

By finally smoothing the cyclic periodograms, consistent estimators of the spectra $g_r(f)$ are then obtained. The estimators of the harmonics H_r of the variance σ^2 of a cyclostationary random process can be obtained by first forming a sample variance of the time series $\mathcal{X}_t$. The sample variance is obtained by dividing the time series $\mathcal{X}_t$ into contiguous segments of length τ_0 such that τ_0 is much smaller than the period T of the cyclostationary process, and by calculating the variance σ_I^2 over each segment. Estimators of the harmonics are obtained either by Fourier analyzing the series σ_I^2 or by making a least square fit to σ_I^2 with the appropriate number of harmonics. Note that the definitions of (i) zero-order ($r = 0$) cyclic autocorrelation, (ii) periodogram, and (iii) zero-order harmonic of the variance, coincide with those usually adopted for stationary random processes. Thus, even though a cyclostationary time series is not stationary, the ordinary spectral analysis can be used for obtaining the zero-order spectra. Note, however, that cyclostationary random processes provide more spectral information about the time series they are associated with due to the existence of cyclic spectra with $r > 0$.

As an important and practical application, let us consider a time series y_t consisting of the sum of a stationary random process, n_t, and a cyclostationary one $\mathcal{X}_t$ (i.e. $y_t = n_t + \mathcal{X}_t$). Let the variance of the stationary time series n_t be ν^2 and its spectral density be $\mathcal{E}(f)$. It is easy to see that the resulting process is also cyclostationary. If the two processes are uncorrelated, then the zero-order harmonic Σ_0^2 of the variance of the combined processes is equal to

$$\Sigma_0^2 = \nu^2 + \sigma_0^2, \quad (38)$$

and the zero-order spectrum, $G_0(f)$, of y_t is

$$G_0(f) = \mathcal{E}(f) + g_0(f). \quad (39)$$

The harmonics of the variance as well as the cyclic spectra of y_t with $r > 0$ coincide instead with those of $\mathcal{X}_t$. In other words, the harmonics of the variance and the cyclic spectra of the process y_t with $r > 0$ contain information only about the cyclostationary process $\mathcal{X}_t$, and are not ''contaminated'' by the stationary process n_t.

VI. ANALYTIC STUDY OF THE BACKGROUND SIGNAL

In the case of the ensemble of N WD-WD binaries, the total signal $s(t)$ is given by the following sum:

$$s(t) = \sum_{i=1}^{N} X^{\mathrm{GW}}(t;\mathbf{\Lambda}_i), \quad (40)$$

where $\mathbf{\Lambda}$ represents the set (ϕ_o, ι, ψ, D, β, λ, $\mathcal{M}_c$, ω_s) of

8 parameters characterizing a GW signal. Since N is large, we can expect the parameters of the signals to be randomly distributed and regard the signal $s(t)$ itself as a random process. Its mean, $m(t)$, and its autocorrelation function, $C(t', t)$ can then be calculated by assuming the probability distribution of the vector $\mathbf{\Lambda}$, $P(\mathbf{\Lambda})$, to be the product of the five probability distributions, $P_1(\phi_o)$, $P_2(\iota)$, $P_3(\psi)$, $P_4(D, \beta, \lambda)$, and $P_5(\mathcal{M}_c, \omega_s)$ (as we did in our numerical simulation of the WD-WD background in Sec. III). By assuming the angles ϕ_o and ψ to be uniformly distributed in the interval $[0, 2\pi)$, and $\cos\iota$ to be uniformly distributed in the interval $[-1, 1]$, we can then perform the integrals over the angles ϕ_o, ψ, and ι analytically and obtain the following expressions:

$$m(t) = N\int_V X^{\rm GW}(t)P(\mathbf{\Lambda})d\mathbf{\Lambda} = \frac{N}{8\pi^2}\int_0^{2\pi}d\phi_o\int_0^{2\pi}d\psi\int_{-1}^{1}d\cos\iota \times\int_{V_4}\int_{V_5}X^{\rm GW}(t)P_4P_5dV_4dV_5 = 0, \quad (41)$$

$$C(t', t) = N\int_V X^{\rm GW}(t')X^{\rm GW}(t)P(\mathbf{\Lambda})d\mathbf{\Lambda} = \frac{N}{16\pi^2}\int_0^{2\pi}d\phi_o\int_0^{2\pi}d\psi\int_{-1}^{1}d\cos\iota \times\int_{V_4}\int_{V_5}\Re[A(x, t')A^*(x, t)e^{i[\phi(t)-\phi(t')]}] \times P_4P_5dV_4dV_5. \quad (42)$$

Note that the mean value $m(t)$ is equal to 0 as a consequence of averaging the antenna response over the polarization angle ψ.

In order to gain an analytic insight about the statistical properties of the autocorrelation function $C(t', t)$, in what follows we will adopt the zero-order long-wavelength approximation of the LISA response $X^{\rm GW}(t)$ obtained by fixing $n = 0$ in (7) and using the expression for the complex amplitude $A^{(0)}$ given in Eq. (8). After some long but straightforward algebra, the autocorrelation function, $C(t', t)$, can be written in the following form:

$$C(t', t) = \frac{16}{5}N\int_{V_4}\int_{V_5}x^4h_o^2[u_2(t')u_2(t) + v_2(t')v_2(t) + u_3(t')u_3(t) + v_3(t')v_3(t) - u_2(t')u_3(t) - v_2(t')v_3(t) - u_3(t')u_2(t) - v_3(t')v_2(t)] \times\cos[\phi(t') - \phi(t)]P_4P_5dV_4dV_5, \quad (43)$$

where $x = \omega_s L$, and $h_o = 4\mathcal{M}_c^{5/3}/D[\omega_s/2]^{2/3}$ (units in which the gravitational constant, G, and the speed of light, c, are equal to 1). For frequencies less than 1 mHz the Doppler modulation in the phase $\phi(t)$ can be neglected making $\phi(t) \simeq \omega_s t$. If we now introduce a new time variable $\tau = t' - t$ and define $B(t, \tau) \equiv C(t + \tau, t)$, we have

$$B(t, \tau) = \int_0^\infty \mathcal{P}(\omega_s)\cos(\omega_s\tau)d\omega_s\sum_{r=-8}^{8}B_r(\tau)e^{ir\Omega t}, \quad (44)$$

where

$$\mathcal{P}(\omega_s) = \frac{48N}{5}(\omega_s L)^4\omega_s^{4/3} \times\int_{\mathcal{M}_c}(\sqrt{2}\mathcal{M}_c)^{10/3}P_5(\mathcal{M}_c, \omega_s)d\mathcal{M}_c, \quad (45)$$

and

$$B_r(\tau) = \int_{V_4}b_r(\Omega\tau)\frac{P_4(D, \beta, \lambda)}{D^2}dV_4. \quad (46)$$

The functions b_r entering into Eq. (46) are equal to

$$\begin{aligned}
b_0 &= V_0^2 + U_0^2 + (V_1^2 + U_1^2)\cos(\Omega\tau) + U_2^2\cos(2\Omega\tau) + (V_3^2 + U_3^2)\cos(3\Omega\tau) + (V_4^2 + U_4^2)\cos(4\Omega\tau) \\
&\quad + (V_0^2 - U_0^2)\cos(4\gamma_0), \\
b_1 &= e^{i(\Omega\tau/2-\delta_0)}[(U_0U_1 + V_0V_1)\cos(\Omega\tau/2) + U_1U_2\cos(3\Omega\tau/2) + U_2U_3\cos(5\Omega\tau/2) \\
&\quad + (U_3U_4 + V_3V_4)\cos(7\Omega\tau/2) + (-U_0U_1 + V_0V_1)\cos(\Omega\tau/2)e^{i4\gamma_0}], \\
b_2 &= e^{i(\Omega\tau-2\delta_0)}[U_0U_2\cos(\Omega\tau) + U_2U_4\cos(3\Omega\tau) + (V_1V_3 + U_1U_3)\cos(2\Omega\tau) \\
&\quad + (-U_1^2/2 + V_1^2/2 - U_0U_2\cos(\Omega\tau))e^{i4\gamma_0}], \\
b_3 &= e^{i3(\Omega\tau/2-\delta_0)}[(U_0U_3 + V_0V_3)\cos(3\Omega\tau/2) + (U_1U_4 + V_1V_4)\cos(5\Omega\tau/2) + ((-U_0U_3 + V_0V_3)\cos(3\Omega\tau/2) \\
&\quad - U_1U_2\cos(\Omega\tau/2))e^{i4\gamma_0}], \\
b_4 &= e^{i2(\Omega\tau-2\delta_0)}[(U_0U_4 + V_0V_4)\cos(2\Omega\tau) + ((V_1V_3 - U_1U_3)\cos(\Omega\tau) + (V_0V_4 - U_0U_4)\cos(2\Omega\tau) - U_2^2/2)e^{i4\gamma_0}], \\
b_5 &= e^{i5(\Omega\tau/2-\delta_0)+i4\gamma_0}[(V_1V_4 - U_1U_4)\cos(3\Omega\tau/2) - U_2U_3\cos(\Omega\tau/2)], \\
b_6 &= e^{i(3\Omega\tau-6\delta_0+4\gamma_0)}[-U_2U_4\cos(\Omega\tau) - U_3^2/2 + V_3^2/2], \qquad b_7 = e^{i7(\Omega\tau/2-\delta_0)+i4\gamma_0}\cos(\Omega\tau/2)[-U_3U_4 + V_3V_4], \\
b_8 &= e^{i4(\Omega\tau-2\delta_0+\gamma_0)}[-U_4^2/2 + V_4^2/2],
\end{aligned} \quad (47)$$

where $\delta_0 = \lambda - \eta_0$, $\gamma_0 = \lambda - \eta_0 - \xi_0$, and the functions U_i, V_i are give in Eqs. (31)–(39) of [8]. It is easy to see that the

autocorrelation $B(t, \tau)$ is periodic in t with period 1 yr for a fixed τ, making it a cyclostationary random process. Note that, if the ecliptic longitude λ is uniformly distributed, all the coefficients b_r given in Eq. (47) vanish for $r > 0$, and the random process $s(t)$ becomes stationary as the autocorrelation $C(t', t)$ now depends on the time difference $t' - t$.

The nonstationarity of the WD-WD background was first pointed out by Giampieri and Polnarev [24] under the assumption of sources distributed anisotropically, and they also obtained the Fourier expansion of the sample variance and calculated the Fourier coefficient for simplified WD-WD binary distributions in the galactic disc. What was however not realized in their work is that this nonstationary random process is actually cyclostationary, i.e. there exists cyclic spectra that can in principle allow us to infer more information about the WD-WD background than one could obtain by just estimating the zero-order spectrum.

If we now set $\tau = 0$ in Eq. (46) we obtain the Fourier expansion of the variance $\sigma^2(t)$ of the cyclostationary process

$$\sigma^2(t) = B(t, 0) = \sum_{k=-8}^{8} B_{k0} e^{ik\Omega t}, \tag{48}$$

where

$$B_{k0} = \mathcal{P}_o \int_{V_5} b_{k0} \frac{P_4(D, \beta, \lambda)}{D^2} dV_4, \tag{49}$$

with $\mathcal{P}_o = \frac{1}{2\pi} \int_0^\infty \mathcal{P}(\omega_s) d\omega_s$, and

$$b_{00} = U_0^2 + U_1^2 + U_2^2 + U_3^2 + U_4^2 + V_0^2 + V_1^2 + V_3^2 + V_4^2 + (V_0^2 - U_0^2)\cos(4\gamma_0), \tag{50}$$

$$b_{10} = e^{-i\delta_0}(U_0U_1 + U_1U_2 + U_2U_3 + U_3U_4 + V_0V_1 + V_3V_4 + (-U_0U_1 + V_0V_1)e^{i4\gamma_0}), \tag{51}$$

$$b_{20} = e^{-i2\delta_0}(U_0U_2 + U_1U_3 + U_2U_4 + V_1V_3 + (-U_1^2/2 + V_1^2/2 - U_0U_2)e^{i4\gamma_0}) \tag{52}$$

$$b_{30} = e^{-i3\delta_0}(U_0U_3 + U_1U_4 + V_0V_3 + V_1V_4 + (-U_0U_3 - U_1U_2 + V_0V_3)e^{i4\gamma_0}) \tag{53}$$

$$b_{40} = e^{-i4\delta_0}(U_0U_4 + V_0V_4 + (-U_0U_4 - U_1U_3 + V_0V_4 + V_1V_3 - U_2^2/2)e^{i4\gamma_0}), \tag{54}$$

$$b_{50} = e^{i(4\gamma_0 - 5\delta_0)}(-U_1U_4 - U_2U_3 + V_1V_4), \tag{55}$$

$$b_{60} = e^{i(4\gamma_0 - 6\delta_0)}(-U_2U_4 - U_3^2/2 + V_3^2/2), \tag{56}$$

$$b_{70} = e^{i(4\gamma_0 - 7\delta_0)}(-U_3U_4 + V_3V_4), \tag{57}$$

$$b_{80} = e^{i(4\gamma_0 - 8\delta_0)}(-U_4^2/2 + V_4^2/2). \tag{58}$$

If we assume the function $\mathcal{P}(\omega_s)$ to change very little over a frequency bin, or equivalently choose τ to be such that $\Omega\tau \ll 1$, we can then approximate the functions b_r with the functions b_{r0}. Under this approximation the cyclic spectra of the process $s(t)$ can be shown to reduce to the following expression:

$$g_r(\omega_s) = \tfrac{1}{2}\mathcal{P}(\omega_s)B_{r0}. \tag{59}$$

Thus under the above approximations the cyclic spectra are determined by one function of the Fourier frequency, and by the coefficients of the Fourier decomposition of the cyclic variance. Note that this simplified representation of the cyclic spectra will not be valid if there are additional correlations between the parameters of the binary population. For example, if the chirp masses or the frequencies of the radiation emitted by the binaries are correlated with the positions of the binaries themselves in the galactic disc, then the cyclic spectra will display a different frequency dependence from that implied by Eq. (59). In general we can expect the direct measurements of the cyclic spectra from the LISA data to allow us to infer properties of the distribution of the parameters characterizing the WD-WD population. In other words, by analyzing the 17 real and independent cyclic spectra we should be able to derive more information about the WD-WD binary population than we would have by simply looking at the ordinary spectrum.

VII. DATA ANALYSIS OF THE BACKGROUND SIGNAL

We have numerically implemented the methods outlined in Sec. V and applied them to our simulated WD-WD background signal. A comparison of the results of our simulation of the detached WD-WD background with the calculation of the background by Hils and Bender [19,29] is shown in Fig. 9. We find that the amplitude of the background from our simulation is a factor of more than 2 smaller than that of Hils and Bender. The level of the WD-WD background is determined by the number of such systems in the Galaxy. We estimate that our number WD-WD binaries should be correct within a factor 5 and thus the amplitude of the background should be right within a factor of $\sqrt{5}$. In Fig. 9 we have plotted the two backgrounds against the LISA spectral density and we have also included the LISA sensitivity curve. The latter is obtained by dividing the instrumental noise spectral density by the detector GW transfer function averaged over isotropically distributed and randomly polarized signals. In the zero-order long-wavelength approximation this averaged transfer function is equal to $\sqrt{3/20}$.

Our analysis was applied to 3 yr of LISA X data consisting of a coherent superposition of signals emitted by detached WD-WD binaries, by semidetached binaries (AM CVn systems), and of simulated instrumental noise. The noise was numerically generated by using the spectral

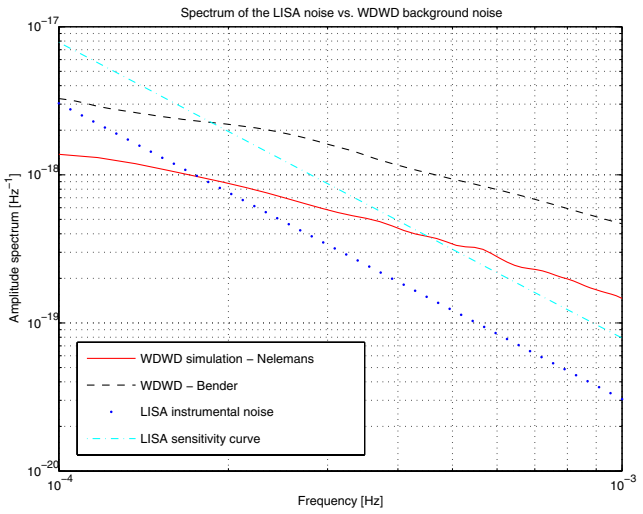

FIG. 9 (color online). Comparison of detached WD-WD background obtained from binary population synthesis simulation ([2,18]) with the WD-WD background calculated by Hils and Bender [19]. The amplitude spectral density of the LISA instrumental noise and the LISA sensitivity curve are drawn for comparison. All spectral densities are one-sided.

density of the TDI X observable given in [12]. In addition a 1 mHz low-pass filter was applied to our data set in order to focus our analyses to the frequency region in which the WD-WD stochastic background is expected to be dominant.

The results of the Fourier analysis of the sample variance of the background signal are shown in Figs. 10 and 11. The top panel of Fig. 10 shows the sample variance of the simulated data for which the variances were estimated over a period of 1 week; periodicity is clearly visible. The bottom panel instead shows the Fourier analysis of the sample variance for which we have removed the mean from the sample variance time series. The vertical lines correspond to multiples of 1 yr; two harmonics can clearly be distinguished from noise. The other peaks of the spectrum that fall roughly half way between the multiples of $1/\mathrm{yr}$ frequency, are from the rectangular window inherent to the finite-time series. In Fig. 11 we present the least square fit of 8 harmonics to our 3 yr of simulated X data. The number 8 comes from our theoretical predictions of the number of harmonics obtained in Sec. VI [see Eq. (44)]. We have calculated the magnitude of the harmonics and obtained the residuals. The results from the least square fit agree very well with those obtained via Fourier analysis (see also Fig. 12). The magnitudes of the first and second harmonics resolved by Fourier analysis, for instance, agree with the corresponding least square fit estimates within a few hundredth of a percent.

It is useful to compare the results of our numerical analysis against the analytic calculations of Giampieri and Polnarev [24]. Their analytic expressions for the harmonics of the variance of a background due to binary

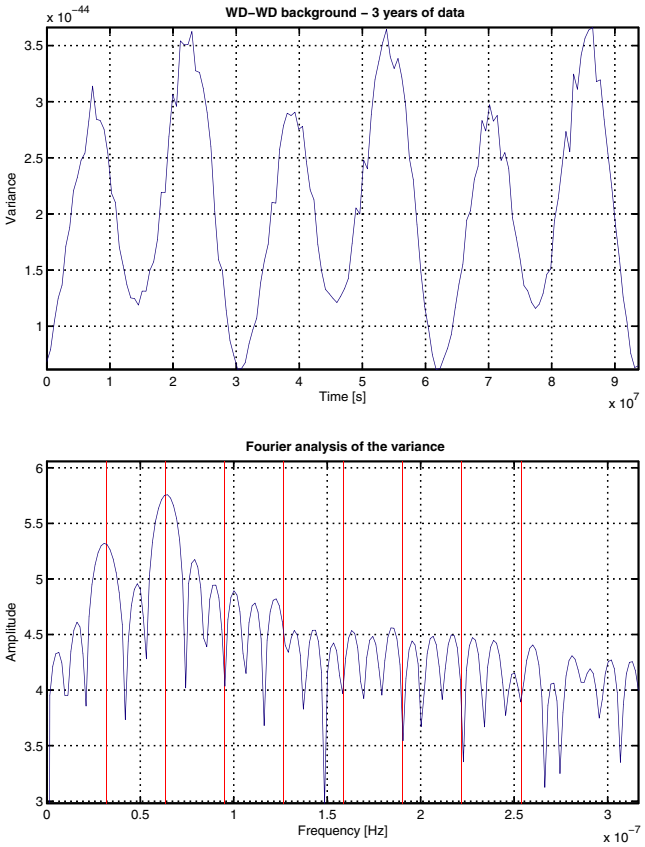

FIG. 10 (color online). Top panel: The sample variance of the simulated WD-WD background observed by LISA. The data includes two populations of WD-WD binaries, detached and semidetached, which are added to the LISA instrumental noise. The data is passed through a low-pass filter with a cutoff frequency of 1 mHz. Bottom panel: Fourier analysis of the sample variance. Two harmonics are clearly resolved.

systems distributed in the galactic disc are given in Eq. (42) and shown in Fig. 4 of [24]. Our estimation roughly matches theirs in that the 0th order harmonics is dominant and the first two harmonics have more power than the remaining ones. Our estimate of the power in the second harmonic, however, is larger than that in the first one, whereas they find the opposite. We attribute this difference to their use of a Gaussian distribution of sources in the galactic disc rather than the exponential that we adopted from [2]. Comparison between these two results suggests that it should be possible to infer the distribution of WD-WD binaries in our Galaxy by properly analyzing the harmonics of the variance of the galactic background measured by LISA. How this can be done will be the subject of a future work.

In order to validate our simulation and data analysis method we have compared the results of our estimation of the power in the harmonics of the variance against the explicit analytic calculation. To estimate the powers we have used Eq. (49) and we have evaluated the integrals by numerical and Monte Carlo methods. In the numerical

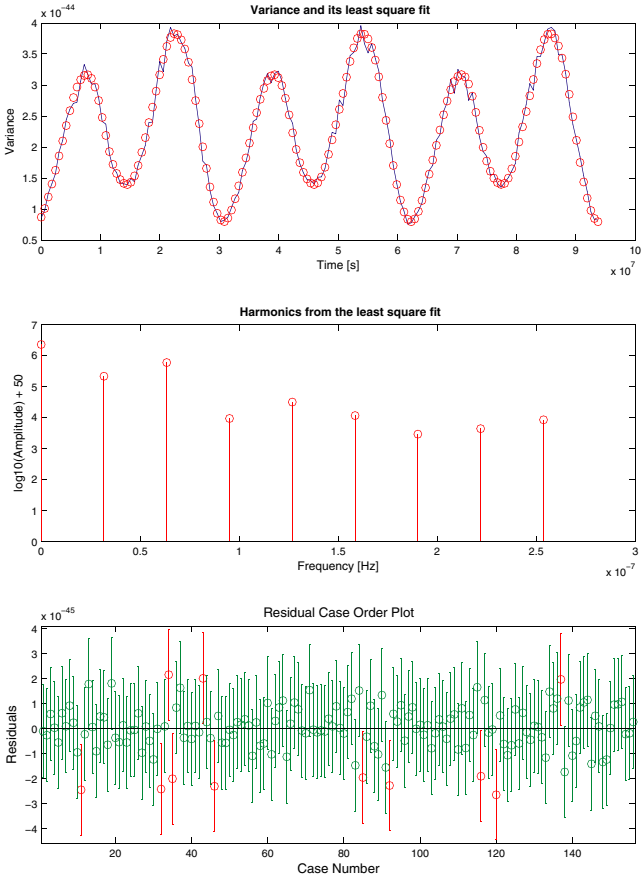

FIG. 11 (color online). Top panel: The sample variance of the WD-WD background data and the least square fit to it using 8 harmonics (small circles). Middle panel: magnitude of the harmonics obtained from the least square fit. Bottom panel: residual error between the fit and the data.

calculation of the harmonics we have limited our analysis to the population of detached WD-WD binaries. Thus in order to make the comparison meaningful we have performed Fourier analysis and least square fit of the time series consisting only of simulated detached WD-WD binaries (without semidetached ones and LISA instrumental noise). The results of the comparison are given in Fig. 12. We see that for the 0th order harmonic and the first two harmonics the agreement is very good. For higher order harmonics there are large discrepancies between the numerical calculation and estimation by the least square fit, while by using the Fourier transform method, we cannot even resolve higher harmonics in our 3-yr data set. We conclude that only the two first harmonics can be extracted reliably from the data. We also observe a very good agreement between the Fourier and the least square method. As a next step in our analysis, we have estimated the cyclic spectra of the simulated WD-WD background signal. In Fig. 13 we have shown the cyclic spectra estimated from the data. We have also plotted the spectrum of the LISA instrumental noise and the main spectrum ($k = 0$) estimated from the simulation. We find that the main spectrum

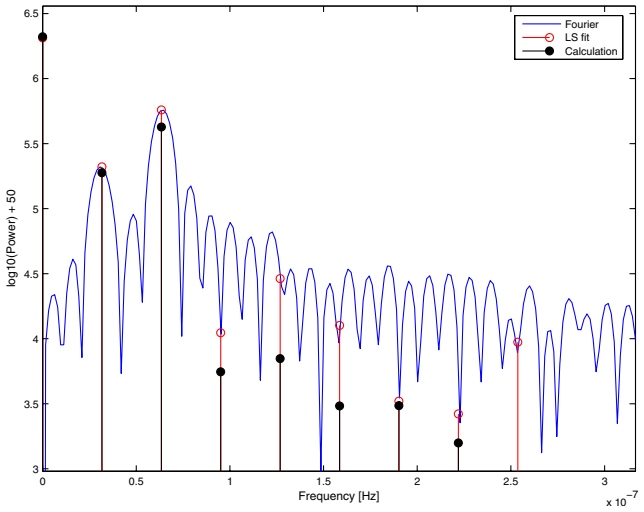

FIG. 12 (color online). Comparison between the estimated power in the harmonics obtained via (i) Fourier analysis, (ii) least square fit, and (iii) numerical calculation based on Eq. (49). The continuous line is the power spectrum of the variance of the data, open circles are obtained from least square fit and the solid circles are from the numerical calculation.

and two cyclic spectra for $k = 1$ and $k = 2$ have the largest magnitude and, over some frequency range, they lie above the LISA instrumental noise. The remaining spectra are an order of magnitude smaller and are very noisy. We also see that all the cyclic spectra have roughly the same slope. This is predicted by our analytic calculations in Sec. VI and it

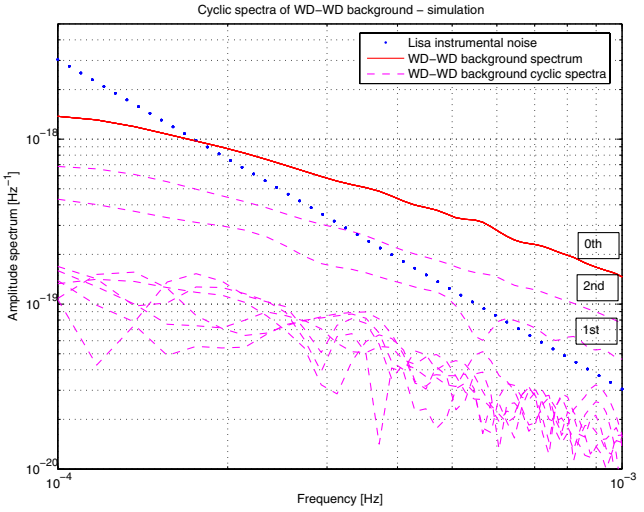

FIG. 13 (color online). The main ($k = 0$) spectrum of the simulated WD-WD background signal (continuous line), and the 8 cyclic spectra (dashed lines) estimated from the simulated data are shown. The spectral density of the LISA instrumental noise (dotted line) is shown for reference. The main, the first and the second order cyclic spectra are flagged. Note that the magnitude of the second cyclic spectrum is larger than the first one.

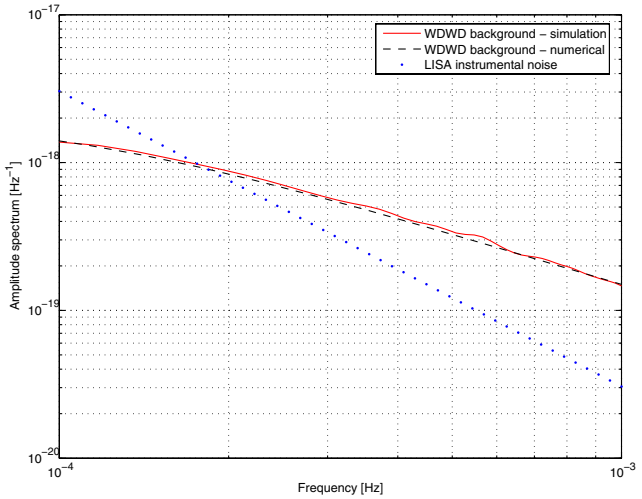

FIG. 14 (color online). Estimated main ($k = 0$) spectrum of the WD-WD background (continuous line) against the calculated spectrum (dashed line). The LISA spectral density curve (dotted line) is shown for comparison. The 0th order spectrum contains the LISA instrumental and hence it differs from the spectrum given in Fig. 9.

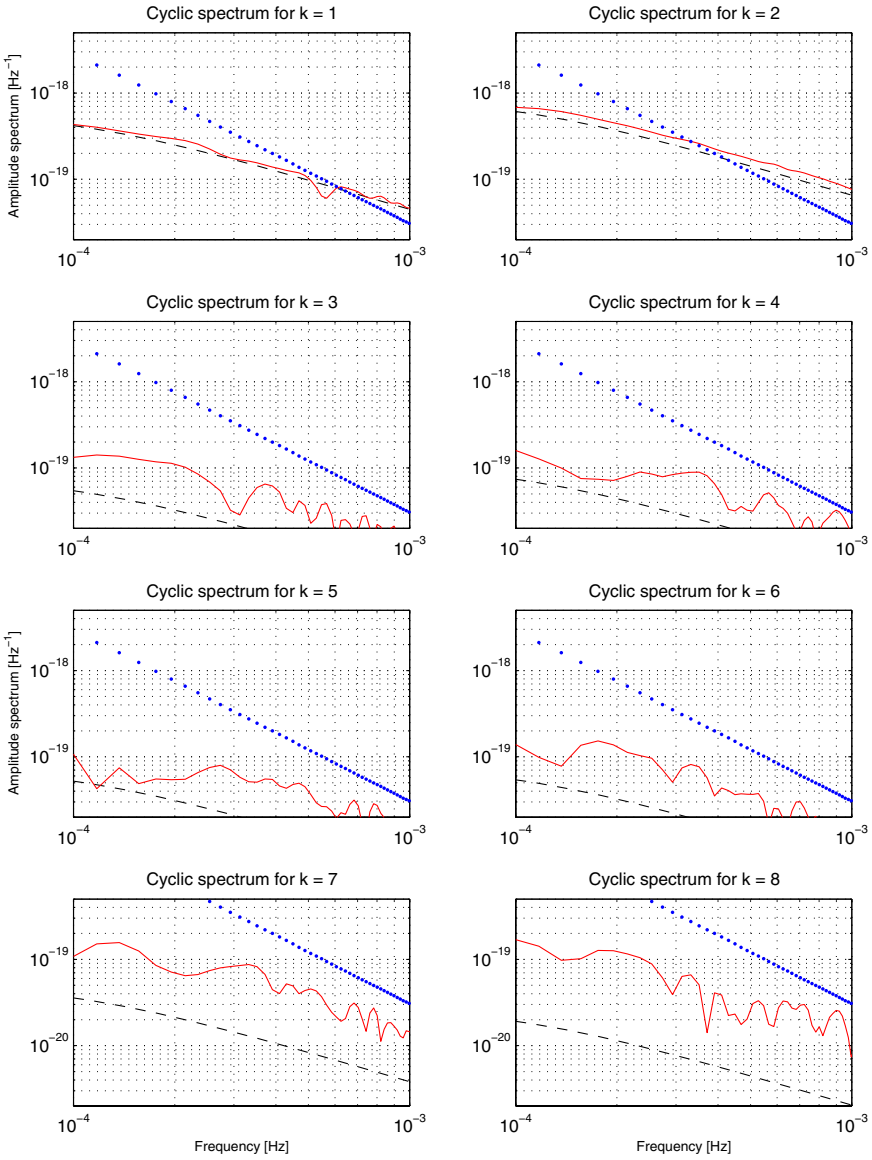

FIG. 15 (color online). Estimated cyclic spectra (continuous lines) against the calculated spectra (dashed line). The LISA spectral density curve (dotted line) is shown for comparison.

follows from the assumed independence between the location of the binaries in the Galaxy (D, λ, β) and their frequencies and chirp masses $(\omega_s, \mathcal{M}_c)$. We also find the magnitude of the 2nd cyclic spectrum to be higher than the first, similarly to what we had for the harmonics of the variance. Note that we estimated the spectra from the time series consisting of the WD-WD background added to the LISA instrumental noise. Like the analysis we did for the variance, we have also compared the estimates of the cyclic spectra from our simulation against those obtained via numerical calculation of the equations derived in Sec. VI. The corresponding results are presented in Figs. 14 and 15, where it is shown that the agreement between the two is quite good.

Our analysis has shown that the LISA data will allow us to compute 17 independent cyclic spectra [the 8 complex cyclic spectra $g_r(f), r = 1, 2, ...8$ and the real spectrum $g_0(f)$] of the WD-WD galactic background, 5 of which can be expected to be measured reliably. We have also shown that by performing generalized spectral analysis of the LISA data we will be able to derive more information about the WD-WD binary population (properties of the distribution of its parameters) than we would have by only looking at the ordinary $g_0(f)$ spectrum.

ACKNOWLEDGMENTS

The supercomputers used in this investigation were provided by funding from the Jet Propulsion Laboratory Institutional Computing and Information Services, and the NASA Directorates of Aeronautics Research, Science, Exploration Systems, and Space Operations. A. K. acknowledges support from the National Research Council under the Resident Research Associateship program at the Jet Propulsion Laboratory. This work was supported in part by the Polish Science Committee Grant No. KBN 1 P03B 029 27. This research was performed at the Jet Propulsion Laboratory, California Institute of Technology, under contract with the National Aeronautics and Space Administration.

[1] P. L. Bender, K. Danzmann, and the LISA Study Team, Max-Planck-Institüt für Quantenoptik Pre-Phase A Report No. MPQ 233, 1998.
[2] G. Nelemans, L. R. Yungelson, and S. F. Portegies-Zwart, Astron. Astrophys. **375**, 890 (2001).
[3] D. Hils, P. L. Bender, and R. F. Webbink, Astrophys. J. **360**, 75 (1990).
[4] Ch. Evans, Ickp Iben, and L. Smarr, Astrophys. J. **323**, 129 (1987).
[5] N. J. Cornish and S. L. Larson, Phys. Rev. D **67**, 103001 (2003).
[6] A. Krolak and M. Tinto, in *Proceedings of the Tenth Marcel Grossmann Meeting on General Relativity*, edited by M. Novello, S. Perez-Bergliaffa, and R. Ruffini (World Scientific, Singapore, 2005).
[7] N. Seto, Phys. Rev. D **69**, 123005 (2004).
[8] A. Królak, M. Tinto, and M. Vallisneri, Phys. Rev. D **70**, 022003 (2004).
[9] M. Tinto, F. B. Estabrook, and J. W. Armstrong, Phys. Rev. D **65**, 082003 (2002).
[10] D. A. Shaddock, Phys. Rev. D **69** , 022001 (2004).
[11] M. Tinto, F. B. Estabrook, and J. W. Armstrong, Phys. Rev. D **69**, 082001 (2004).
[12] F. B. Estabrook, M. Tinto, and J. W. Armstrong, Phys. Rev. D **62**, 042002 (2000).
[13] J. W. Armstrong, F. B. Estabrook, and M. Tinto, Astrophys. J. **527**, 814 (1999).
[14] D. A. Shaddock, M. Tinto, F. B. Estabrook, and J. W. Armstrong, Phys. Rev. D **68**, 061303(R) (2003).
[15] N. J. Cornish and R. W. Hellings, Classical Quantum Gravity **22**, 4851 (2003).
[16] L. J. Rubbo, N. J. Cornish, and O. Poujade, Phys. Rev. D **69**, 082003 (2004).
[17] M. Tinto and S. L. Larson, Phys. Rev. D **70**, 062002 (2004).
[18] G. Nelemans, L. R. Yungelson, and S. F. Portegies-Zwart, Mon. Not. R. Astron. Soc. **349**, 181 (2004).
[19] P. L. Bender and D. Hils, Classical Quantum Gravity **14**, 1439 (1997).
[20] D. Hils and P. L. Bender, Astrophys. J. **537**, 334 (2000).
[21] P. L. Bender and D. Hils, Classical Quantum Gravity **14**, 1439 (1997).
[22] T. R. Marsh, G. Nelemans, and D. Steeghs, Mon. Not. R. Astron. Soc. **350**, 113 (2004).
[23] *Handbook of Mathematical Functions with Formulas, Graphs, and Mathematical Tables*, edited by M. Abramowitz and I. A. Stegun (Dover, New York, 1972), 9th ed., pp. 355–389.
[24] G. Giampieri and A. G. Polnarev, Mon. Not. R. Astron. Soc. **291**, 149 (1997).
[25] A. H. Nuttall, IEEE Transactions on Acoustics, Speech, and Signal Processing **29**, 84 (1981).
[26] Michele Vallisneri (private communication).
[27] H. L. Hurd, IEEE Trans. Inf. Theory **35**, 350 (1989).
[28] D. B. Percival and A. T. Walden, *Spectral Analysis for Physical Applications* (Cambridge University Press, Cambridge, United Kingdom, 1993), Chap. 6.
[29] Plots and data for LISA sensitivity curve and WD-WD background due to Hils and Bender can be found at the following URL: http://www.srl.caltech.edu/shane/sensitivity/MakeCurve.html.